


## Effect of spin-orbit coupling in noncentrosymmetric half-Heusler alloys

Kunal Dutta, Subhadeep Bandyopadhyay,<sup>\*</sup> and Indra Dasgupta<sup>†</sup>  
*School of Physical Sciences, Indian Association for the Cultivation of Science,  
 2A and 2B Raja S.C. Mullick Road, Jadavpur, Kolkata 700 032, India*

 (Received 7 July 2023; revised 18 October 2023; accepted 22 November 2023; published 19 December 2023)

The spin-orbit coupled electronic structure of two representative nonpolar half-Heusler alloys, namely 18-electron compound CoZrBi and 8-electron compound SiLiIn, has been studied in detail. An excursion through the Brillouin zone of these alloys from one high-symmetry point to the other revealed rich local symmetry of the associated wave vectors resulting in nontrivial spin splitting of the bands and consequent diverse spin textures in the presence of spin-orbit coupling. Our first-principles calculations supplemented with the low-energy  $\mathbf{k} \cdot \mathbf{p}$  model Hamiltonian revealed the presence of the linear Dresselhaus effect at the  $X$  point having  $D_{2d}$  symmetry, and the Rashba effect with both linear and nonlinear terms at the  $L$  point with  $C_{3v}$  point group symmetry. Interestingly we have also identified nontrivial Zeeman spin splitting at the non-time-reversal invariant  $W$  point and a pair of nondegenerate bands along the path  $\Gamma$  to  $L$  displaying vanishing spin polarization due to the non-pseudo-polar point group symmetry of the wave vectors. Further, a comparative study of CoZrBi and SiLiIn suggests, in addition to the local symmetry of the wave vectors, the important role of the participating orbitals in deciding the magnitude of the spin splitting of the bands. Our calculations suggest that half-Heusler compounds with heavy elements displaying diverse spin textures may be ideal candidates for spin valleytronics, where spin textures can be controlled by accessing different valleys around the high-symmetry  $k$ -points.

DOI: [10.1103/PhysRevB.108.245146](https://doi.org/10.1103/PhysRevB.108.245146)

### I. INTRODUCTION

In noncentrosymmetric systems, the nonvanishing gradient of the electrostatic potential results in a momentum-dependent magnetic field  $\mathbf{\Omega}(\mathbf{k})$  in the rest frame of the electron. The coupling of this field with the spin  $\vec{\sigma}$  of the electron lifts the spin-degeneracy of the bands in an otherwise nonmagnetic system. The resulting spin-orbit coupled Hamiltonian is given by  $H_{\text{SOC}} = \mathbf{\Omega}(\mathbf{k}) \cdot \vec{\sigma}$ . Depending on the symmetry,  $\mathbf{\Omega}(\mathbf{k})$  may have both linear and higher-order  $k$ -dependent terms. The momentum-dependent field  $\mathbf{\Omega}(\mathbf{k})$  that locks the electron's spin direction to its momentum not only removes the spin degeneracy of the bands but also leads to complex spin textures in the reciprocal space. Spin texture (ST) is the expectation value of the spin operator  $\langle \vec{S}_n(\mathbf{k}) \rangle$  in a given Bloch wave function  $u_n(\mathbf{k})$  around a specific  $k$ -point, where  $n$  is the band index. Spin textures depending on the symmetry may display Rashba [1], Dresselhaus [2], persistent [3], radial [4], or more complex spin configurations in the momentum space. In addition to the well-studied Dresselhaus and Rashba effect that leads to splitting of nondegenerate bands with characteristic ST in noncentrosymmetric systems, there are also other possibilities where spin degeneracy can be lifted in nonmagnetic, noncentrosymmetric systems due to the presence of  $\mathbf{\Omega}(\mathbf{k})$ .

It is well known that in materials either with intrinsic magnetic ordering or in the presence of a magnetic field,

time reversal (TR) symmetry is broken, leading to splitting of energy bands with opposite spins, referred to as Zeeman spin splitting [5]. In nonmagnetic, noncentrosymmetric compounds, a combination of non-time-reversal invariant  $k$ -point and lack of inversion symmetry in the presence of spin-orbit coupling (SOC) also leads to spin splitting of bands in the momentum space similar to the Zeeman effect [6]. Further, the possibility of spin splitting of bands in a nonmagnetic, noncentrosymmetric crystal in the presence of SOC has recently been shown, where the split bands do not show any net spin polarization around certain high-symmetry points of the Brillouin zone (BZ) [7]. Such systems with band splitting having vanishing spin polarization offer the possibility of tuning spin polarization either with the application of an electric field or strain that may be important for spintronics application.

Earlier research on the Dresselhaus effect was primarily focused on materials in which the bulk exhibits inversion asymmetry. It was originally proposed for nonpolar zincblende semiconductors, where the splitting of the band is proportional to  $k^3$  [2]. On the other hand, the Rashba effect was proposed for noncentrosymmetric polar wurtzite structure displaying linear splitting of bands [8]. The search for the Rashba effect was initially confined to two-dimensional (2D) surfaces, interfaces. In view of the above, Rashba splitting was observed on surfaces of heavy metals, such as Au (111) [9] and Bi (111) [10], at the surface of oxides such as SrTiO<sub>3</sub> (001) [11] and KTaO<sub>3</sub> (001) [12], on two-dimensional materials [13–15], and on heterostructure interfaces such as InGaAs/InAlAs [16] and LaAlO<sub>3</sub>/SrTiO<sub>3</sub> [17]. However, recent studies on bulk polar materials show large Rashba spin splitting for, e.g., in BiTeX ( $X = \text{Cl, Br, I}$ ) [18–20] and GeTe

<sup>\*</sup>Present address: Theoretical Materials Physics, CESAM, University of Liège, Liège, Belgium.

<sup>†</sup>sspid@iacs.res.in

[21,22]. Recently it has been reported that both Dresselhaus and Rashba spin splitting is also observed in bulk ferroelectric oxide perovskites such as BiAlO<sub>3</sub> [23], HfO<sub>2</sub> [24], and nitride perovskite LaWN<sub>3</sub> [25]. Further recent studies suggest that not only does the Rashba effect occur in bulk for polar and ferroelectric crystal structures, but it may also occur in nonpolar crystals with polar point group in the BZ [26]. The Zeeman effect, on the other hand, was observed in the two-dimensional WSe<sub>2</sub> and MoS<sub>2</sub> [27,28], and a large Zeeman splitting was also observed in bulk OsC, WN<sub>2</sub>, SnTe [29], and in the nonpolar GaAs [30]. Band splitting with vanishing spin polarization was suggested to be realized in bulk nonsymmorphic GaAs and symmorphic 2D-SnTe [7].

While crystallographic point group symmetry (CPGS) was originally attributed to being responsible for the nature of spin textures (Rashba- or Dresselhaus-type), very recently it was observed that the point group symmetry of the wave vector (little group) [26] and the symmetry of the orbitals involved [31] play a crucial role in determining the spin textures. As a consequence, in the same compound diverse spin textures can be realized around different high-symmetry  $k$ -points of the BZ depending on its little group. Similarly different compounds at a particular  $k$ -point despite having the same little group, depending on the orbital character of the bands, may display diverse spin textures [31].

In this paper, we have considered two representative semiconducting half-Heusler compounds with heavy elements having 18 and 8 valance electrons, respectively. The unique nonpolar crystal structure of the half-Heusler compounds where the ternary half-Heusler is a combination of two binaries, one with centrosymmetric and the other with non-centrosymmetric structure, will be shown to host a variety of spin textures depending on the symmetry of the  $k$ -points in the BZ. Our calculations clearly identify the importance of the little group of the chosen  $k$ -point in determining the nature of the spin textures. A comparative study of the two half-Heusler compounds shows that the orbital character of the bands is important in deciding the strength of the SOC induced band splitting.

The rest of the paper is organized as follows. Section II is devoted to a description of the structural properties of nonpolar half-Heusler compounds and details of the computational methods. In Sec. III we have discussed the results of our first-principles electronic structure calculations. Section IV is devoted to a description of the nature of band splitting and consequent spin textures at various high-symmetry  $k$ -points of the BZ. The results of our first-principles calculations have been analyzed here in the framework of a low-energy  $\mathbf{k} \cdot \mathbf{p}$  model. Finally, conclusions are presented in Sec. V.

## II. STRUCTURAL AND COMPUTATIONAL DETAILS

The half-Heusler compound XYZ crystallizes in the face-centered-cubic structure with one formula unit per primitive unit cell, as shown in Fig. 1(a). In normal half-Heusler alloys, X and Y are transition metals, with X being a higher valence element in comparison to Y, and Z is an  $sp$  valent element. The space group is  $F\bar{4}3m$  (no. 216). In the conventional stable structure Y and Z atoms are located at  $4a(0, 0, 0)$  and  $4b(\frac{1}{2}, \frac{1}{2}, \frac{1}{2})$  positions forming the rocksalt

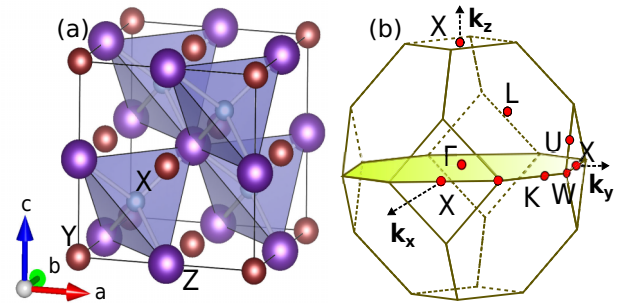


FIG. 1. (a) Crystal structure and (b) BZ of bulk half-Heusler compounds. The half-Heusler compound have XYZ composition, where X (Co, Si) have higher valence compared to Y (Zr, Li), and Y and Z (Bi, In) form a rocksalt structure.

structure arrangement and the X atom is located in the tetrahedrally coordinated pocket, at one of the cube center positions  $4c(\frac{1}{4}, \frac{1}{4}, \frac{1}{4})$  leaving the other  $4c(\frac{3}{4}, \frac{3}{4}, \frac{3}{4})$  empty, resulting in the absence of inversion symmetry. We shall consider a representative semiconducting 18 valence electron half-Heusler compound CoZrBi [32]. In addition, we have also considered a representative semiconducting  $sp$  valent compound SiLiIn [33] featuring half-Heusler structure with eight valence electrons.

The calculations presented in this paper have been carried out using the Vienna *ab initio* simulation package (VASP) [34,35] within density-functional theory (DFT) using the supplied projector augmented-wave pseudopotentials [36,37] and the Perdew-Burke-Ernzerhof generalized gradient approximation (GGA) [38]. Here the energy cutoff has been set to 600 eV for the calculations and a  $10 \times 10 \times 10$   $k$ -point mesh is used for the self-consistent calculations using the Monkhorst grid for  $k$ -point sampling. All the calculations are done with an experimental lattice constant. The details of the structure, including structural parameters, are summarized in Table I.

Figure 1(b) represents the BZ of the face-centered-cubic half-Heusler compound. The various high-symmetry points of the BZ are  $\Gamma$  at the center of the BZ, L at the center of each hexagonal face, X at the center of each square face, W at each corner formed from one square and two hexagons, and K at the middle of an edge joining two hexagonal faces. Further, the X point has sixfold degeneracy, the L point has eightfold degeneracy, and the W and K points have 12-fold degeneracy.

TABLE I. The lattice constant and atomic positions for bulk half-Heusler compounds.

Bulk		Site	$x$	$y$	$z$
Space group	half-Heusler				
$F\bar{4}3m$ (216)	18-electron CoZrBi	Zr(4a)	0.00	0.00	0.00
		Co(4c)	0.25	0.25	0.25
		Bi(4b)	0.50	0.50	0.50
	8-electron SiLiIn	Li(4a)	0.00	0.00	0.00
		Si(4c)	0.25	0.25	0.25
		In(4b)	0.50	0.50	0.50

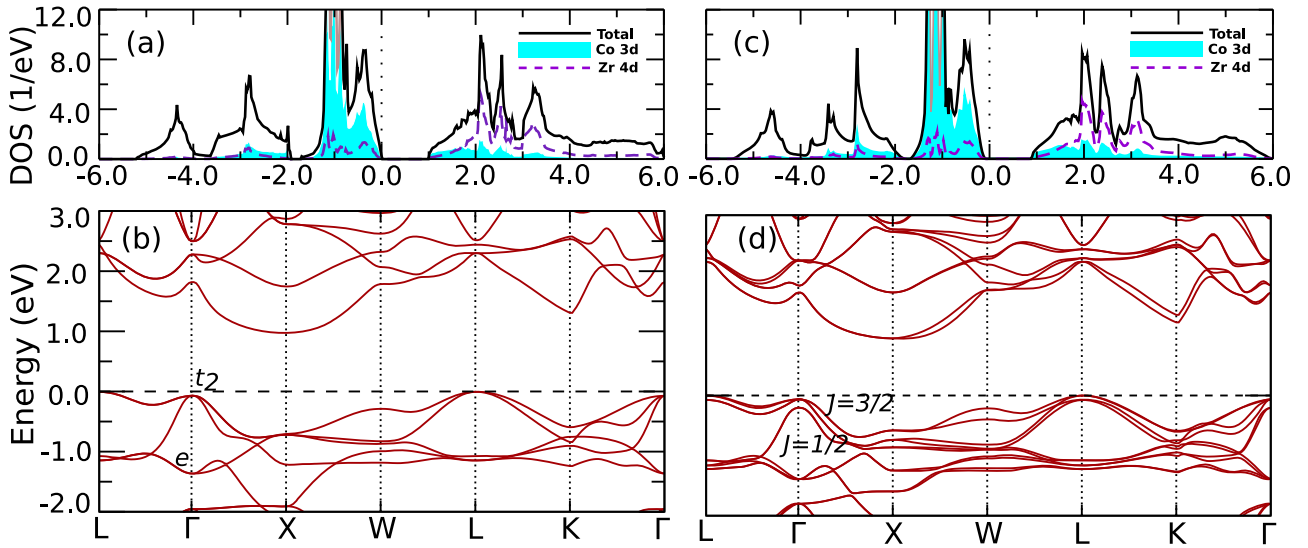


FIG. 2. The density of states and electronic band structure of the 18-electron half-Heusler compound CoZrBi, in the absence and presence of SOC. In (a) and (c) the total and projected DOS for the Co-3d and Zr-4d are shown without and with SOC, respectively. Parts (b) and (d) display the band structure along various high-symmetry points of the BZ in the absence and presence of SOC, respectively. The band structures of CoZrBi are plotted along the high-symmetry points  $L(\frac{\pi}{a}, \frac{\pi}{a}, \frac{\pi}{a})-\Gamma(0, 0, 0)-X(0, \frac{2\pi}{a}, 0)-W(\frac{\pi}{a}, \frac{2\pi}{a}, 0)-L(\frac{\pi}{a}, \frac{\pi}{a}, \frac{\pi}{a})-K(\frac{3\pi}{2a}, \frac{3\pi}{2a}, 0)-\Gamma(0, 0, 0)$  of the BZ. The Fermi level is aligned to the valence-band maximum with zero value in the energy axis.

In the BZ, except for the  $W$  and  $K$  points, all are time-reversal (TR) invariant. A time-reversal-invariant  $k$ -point [39] satisfies the condition  $-\mathbf{k} + \mathbf{G} = \mathbf{k}$ , where  $\mathbf{G}$  is the reciprocal-lattice vector.

### III. ELECTRONIC STRUCTURE CALCULATIONS

To begin with, we have analyzed the density of states without SOC for the 18-electron compound CoZrBi obtained from DFT calculations. The non-spin-polarized total as well as projected densities of states of Co-3d and Zr-4d have been shown in Fig. 2(a). The characteristic feature of the total DOS is a pair of bonding and antibonding states resulting from the covalent hybridization of the higher valence Co- $d$  and lower valence Zr- $d$  states separated by a 0.98 eV gap at the Fermi level [40]. Below the bonding states are the Bi- $p$  states separated by a  $p$ - $d$  gap. Below the Bi- $p$  state lies the Bi- $s$  state. The semiconducting nature of the compound can be understood from the electron filling of the system. As the total number of valence electrons of the system is 18, these are accommodated in the available Bi- $s$ , Bi- $p$ , and the bonding partner of the Co- $d$ -Zr- $d$  hybridized states. The Co- $d$  and Zr- $d$  projected DOS reveal that the bonding states have the primary contribution from the 3d states of Co, while the antibonding states are primarily composed of Zr- $d$  states.

In Fig. 2(b) we have shown the band structure of CoZrBi around the Fermi level. An indirect band gap of 0.98 eV is observed between the  $L$  point of the valence band and the  $X$  point of the conduction band, in agreement with a previous report [41]. Further, due to the tetrahedral network, at the  $\Gamma$  point, the top of the valence band consisting of Co-Zr  $d$ -states splits into threefold-degenerate  $t_2$  and twofold-degenerate  $e$  states, with the latter lying lower in energy.

Figures 2(c) and 2(d) display DOS and the band structure of CoZrBi including SOC. The gross feature of the DOS is very similar to that obtained without SOC, except for the presence of additional splittings, and the value of the  $d$ - $d$  gap is now 0.96 eV. However, the nontrivial effect of the absence of inversion symmetry upon inclusion of SOC is revealed in the band structure shown in Fig. 2(d). The effect of the SOC depends on the symmetry of the paths in the reciprocal space. The spin degeneracy of the bands along various high-symmetry directions of the BZ is lifted. Of particular interest is the top of the valence band at the  $\Gamma$  point, where SOC further splits the  $t_2$  states into fourfold-degenerate  $J = \frac{3}{2}$  and twofold-degenerate  $J = \frac{1}{2}$  states, with the latter lying lower in energy in the tetrahedral environment. Unlike the  $t_2$  states, the  $e$ -states retain their degeneracy at the  $\Gamma$  point.

The total as well as the projected DOS and the band structure around the Fermi level without SOC for the 8-electron half-Heusler SiLiIn is shown in Figs. 3(a) and 3(b), respectively. Similar to the 18-electron compound, the characteristic feature of the DOS is a pair of bonding and antibonding states derived from In  $s + p$  and Si  $s + p$  separated by a semiconducting gap of magnitude 0.12 eV. Below the bonding state lies the Si- $s$  state. As the total number of valence electrons of the system is 8, these are accommodated in the Si- $s$  state and bonding partner of the  $p$ -states below the Fermi level. The plot of the band structure reveals an indirect band gap of 0.12 eV between the  $\Gamma$  point of the valence band and the  $X$  point of the conduction band. The top of the valence band at the  $\Gamma$  point is the threefold-degenerate  $p$ -band. The lowest conduction band is predominantly the  $sp^3$  hybridized In- $s$ -Si- $p$  band [see Fig. 3(b), inset].

Finally, the DOS and band structure of SiLiIn including SOC are shown in Figs. 3(c) and 3(d). The gross feature of the

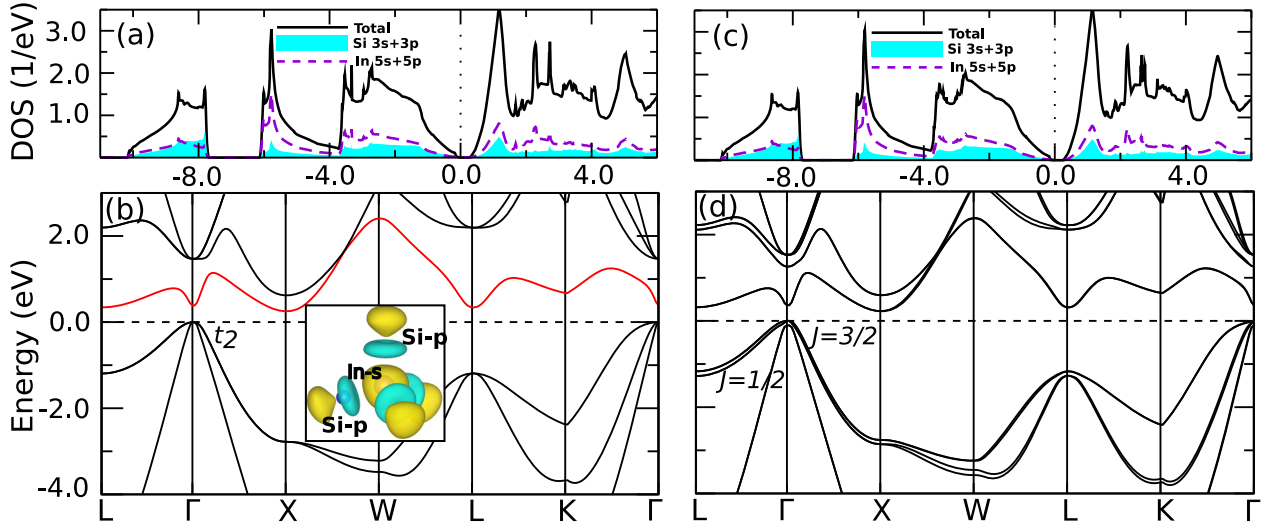


FIG. 3. The density of states and electronic band structure of the 8-electron half-Heusler compound SiLiIn, in the absence and presence of SOC. In (a) and (c) the total and projected DOS for the Si-3s + 3p and In-5s + 5p are shown without and with SOC, respectively. Parts (b) and (d) display the band structure along various high-symmetry points of the BZ in the absence and presence of SOC, respectively. The band structures of SiLiIn are plotted along the high-symmetry points  $L(\frac{\pi}{a}, \frac{\pi}{a}, \frac{\pi}{a})-\Gamma(0, 0, 0)-X(0, \frac{2\pi}{a}, 0)-W(\frac{\pi}{a}, \frac{2\pi}{a}, 0)-L(\frac{\pi}{a}, \frac{\pi}{a}, \frac{\pi}{a})-K(\frac{3\pi}{2a}, \frac{3\pi}{2a}, 0)-\Gamma(0, 0, 0)$  of the BZ. Fermi level is aligned to the valence-band maximum with zero value in the energy axis. The inset in (b) represents the Wannier function of the lowest conduction band.

DOS is very similar to that without SOC shown in Fig. 3(a) except for additional splittings. As expected, around the  $\Gamma$  point of the valence band, the threefold-degenerate  $p$ -bands split into  $J = \frac{3}{2}$  and  $J = \frac{1}{2}$  states, where the splitting is much smaller in comparison to the 18-electron compound.

#### IV. NATURE OF BAND SPLITTING AND SPIN TEXTURES

Next we have analyzed the nature of the SOC-induced splitting of the bands near various high-symmetry points of the BZ, in order to elucidate the importance of local symmetry. In the following, we have discussed in detail the spin orbital locked split bands and the novel spin textures displayed by them in the  $k$ -space at and around the TR invariant nonpolar ( $X$ ), polar ( $L$ ), and non-time-reversal invariant  $W$  points, which, based on local symmetry, are expected to display the Dresselhaus effect, the Rashba effect, and the Zeeman effect, respectively.

##### A. Dresselhaus and Rashba effect

###### 1. $X$ point $(0, 0, \frac{2\pi}{a})$

To begin with, we have analyzed the conduction-band minimum (CBM) of CoZrBi around the neighborhood of the high-symmetry nonpolar  $X$  point along the path  $W(\frac{\pi}{a}, 0, \frac{2\pi}{a})-X(0, 0, \frac{2\pi}{a})-W(0, \frac{\pi}{a}, \frac{2\pi}{a})$  in the  $k_z = \frac{2\pi}{a}$  plane. The DFT band structure for CoZrBi in a narrow  $k$ -range along the above-mentioned path, without and including SOC, are displayed in Figs. 4(a) and 4(b), respectively. The band structure including SOC shows that the band minimum is shifted from the  $X$  point in both directions, reminiscent of the Rashba-Dresselhaus effect. To identify the nature of the spin splitting, the ST of the inner and outer branches of the CBM around the  $X$  point has been shown in Figs. 4(c) and

4(d), respectively. As shown in Figs. 4(c) and 4(d), the angle between the  $\mathbf{k}$  and the expectation values of spin  $\langle S_x \rangle$  and  $\langle S_y \rangle$  varies with the direction and the  $\langle S_z \rangle$  component is absent. Along the  $k_x$  and  $k_y$  axis, the spin is parallel to  $\mathbf{k}$ , while it is perpendicular to  $\mathbf{k}$  along the diagonals. As expected the direction of the spin textures is opposite for the inner and outer branches, as shown in Figs. 4(c) and 4(d), respectively. These are characteristic signatures of the linear Dresselhaus effect. To understand our DFT results next we have derived a low energy  $\mathbf{k} \cdot \mathbf{p}$  model Hamiltonian.

The point-group symmetry around the  $X(0, 0, \frac{2\pi}{a})$  point is  $D_{2d}$  having twofold  $C_2(z)$  rotation around the  $z$  axis (principal axis), twofold rotation perpendicular to the principal axis ( $C'_2(x), C'_2(y)$ ), reflection in the dihedral plane ( $M_{d1}, M_{d2}$ ), and fourfold rotation followed by reflection through a plane perpendicular to the principal axis  $S_4(z)$ . All the symmetries are listed in Table II. The symmetry operations listed in Table II keep the linear Dresselhaus Hamiltonian  $H_D(k)$

TABLE II. Symmetry operations of  $D_{2d}$  point group.

X point		
Symmetry operation	$\{k_x, k_y, k_z\}$	$\{\sigma_x, \sigma_y, \sigma_z\}$
$C_2(z) = -i\sigma_z$	$\{-k_x, -k_y, k_z\}$	$\{-\sigma_x, -\sigma_y, \sigma_z\}$
$C'_2(x) = -i\sigma_x$	$\{k_x, -k_y, k_z\}$	$\{\sigma_x, -\sigma_y, -\sigma_z\}$
$C'_2(y) = -i\sigma_y$	$\{-k_x, k_y, k_z\}$	$\{-\sigma_x, \sigma_y, -\sigma_z\}$
$S_4(z) = e^{i\frac{\pi}{4}\sigma_z}$	$\{k_y, -k_x, k_z\}$	$\{-\sigma_y, \sigma_x, \sigma_z\}$
$M_{d1} = -i(\frac{-\sigma_x + \sigma_y}{\sqrt{2}})$	$\{k_y, k_x, k_z\}$	$\{-\sigma_y, -\sigma_x, -\sigma_z\}$
$M_{d2} = -i(\frac{\sigma_x + \sigma_y}{\sqrt{2}})$	$\{-k_y, -k_x, k_z\}$	$\{\sigma_y, \sigma_x, -\sigma_z\}$

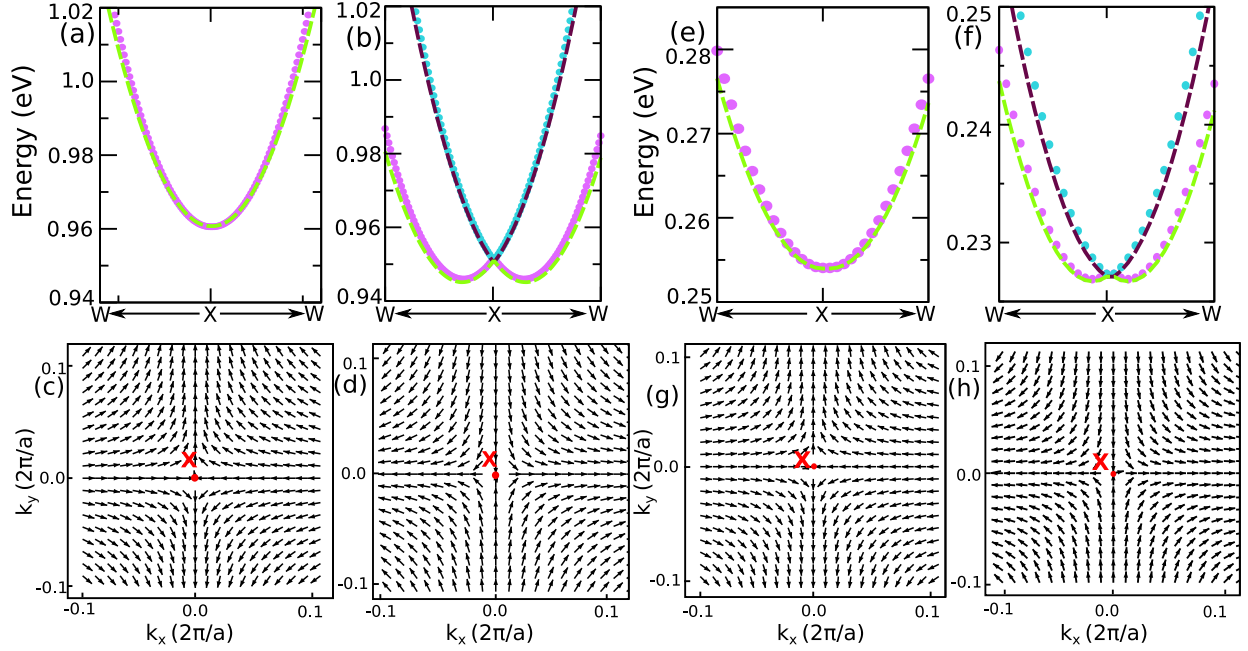


FIG. 4. The band structure and ST of CoZrBi and SiLiIn plotted in the  $k_z = \frac{2\pi}{a}$  plane in a very narrow  $k$ -range around the  $X$  point in the presence and absence of SOC. In (a) and (b), the band structures of CoZrBi without and with SOC plotted along  $\frac{2\pi}{a}(0.3, 0.0, 1.0) - \frac{2\pi}{a}(0.0, 0.0, 1.0) - \frac{2\pi}{a}(0.0, 0.3, 1.0)$  path, which is along the path  $W \leftarrow X \rightarrow W$ . In (e) and (f) the band structures of SiLiIn without and with SOC are plotted along the  $\frac{2\pi}{a}(0.075, 0.0, 1.0) - \frac{2\pi}{a}(0.0, 0.0, 1.0) - \frac{2\pi}{a}(0.0, 0.075, 1.0)$  direction. The band structure obtained from the DFT calculation as plotted with dots while the band structure obtained from the  $\mathbf{k} \cdot \mathbf{p}$  model Hamiltonian is plotted with dashed lines. In (c) and (d), the inner and outer branches of ST of CoZrBi around the  $X$  point in the conduction-band minimum (CBM) are shown. Parts (g) and (h) display the same spin-texture for SiLiIn.

invariant. Further, Table II reveals that the out-of-plane spin component is zero, as no linear combination of  $k_x$  and  $k_y$  with  $\sigma_z$  is invariant under the symmetry operations. The effective Hamiltonian is

$$H_X(k) = H_0(k) + \alpha_D(\sigma_x k_x - \sigma_y k_y), \quad (1)$$

where  $H_0$  is the Hamiltonian of the free electrons with the dispersion  $E_0(k) = \frac{\hbar^2}{2m^*}(k_x^2 + k_y^2 + (\frac{2\pi}{a})^2)$  and  $\alpha_D$  is the Dresselhaus coupling constant. Diagonalization of Eq. (1) yields  $E(k)^\pm = E_0 \pm \alpha_D \sqrt{(k_x^2 + k_y^2)}$ . The band structure obtained from the model Hamiltonian calculation around the  $X$  point without and including SOC is shown with dashed lines in Figs. 4(a) and 4(b), respectively, and it agrees well with the DFT calculations. The value of the Dresselhaus parameter ( $\alpha_D$ ) obtained from the model Hamiltonian is  $\alpha_D = 0.26 \text{ eV \AA}$ . The value of  $\alpha_D$  calculated as twice the ratio between the shift in energy and momentum from DFT calculation,  $\alpha_D = \frac{2\delta E}{\delta k} = 0.25 \text{ eV \AA}$ , is in a good agreement with that obtained from the  $\mathbf{k} \cdot \mathbf{p}$  calculations.

Similarly, for the 8-electron system SiLiIn, the band structure of the CBM around the  $X$  point, in the absence and presence of SOC is displayed in Figs. 4(e) and 4(f), respectively. The band splitting seen in Fig. 4(f) suggests the Rashba-Dresselhaus effect. A comparison of ST shown in Figs. 4(c) and 4(d) with Figs. 4(g) and 4(h) reveals that the ST for 18 and 8 electrons are identical. As expected from the nature of band splitting, the Dresselhaus parameter  $\alpha_D$

is small and estimated to be  $0.08 \text{ eV \AA}$ . This small splitting is attributed to the participation of the  $sp^3$  hybridized states for SiLiIn in contrast to the  $d$  states for CoZrBi, where the strength of SOC is expected to be higher for the latter.

Using the model Hamiltonian Eq. (1), we have calculated the band structure without and with SOC and is shown with dotted line in Figs. 4(e) and 4(f), which agrees well with the band structure obtained from the DFT calculations. The calculated Dresselhaus parameter from the model Hamiltonian,  $\alpha_D = 0.08 \text{ eV \AA}$ , is in excellent agreement with the DFT estimate.

## 2. $L$ point $(\frac{\pi}{a}, \frac{\pi}{a}, \frac{\pi}{a})$

Next we have focused around the polar  $L$  point of the conduction band of the 18-electron half-Heusler compound CoZrBi that features a local maximum. The DFT band structure without and with SOC is plotted in a narrow  $k$ -range around the neighborhood of the high-symmetry  $L(\frac{\pi}{a}, \frac{\pi}{a}, \frac{\pi}{a})$  point along  $W(\frac{2\pi}{a}, 0, \frac{\pi}{a})$  and  $K(\frac{3\pi}{2a}, \frac{3\pi}{2a}, 0)$  directions as shown in Figs. 5(a) and 5(b), respectively. The nature of the SOC-induced band splitting into two branches [see Fig. 5(b)] indicates the presence of either the Rashba or Dresselhaus effect. We shall confirm the nature of the band splitting by calculating the spin textures in the framework of DFT supplemented with symmetry analysis within the  $\mathbf{k} \cdot \mathbf{p}$  model. To facilitate the plot of ST, we have considered a plane  $\perp$

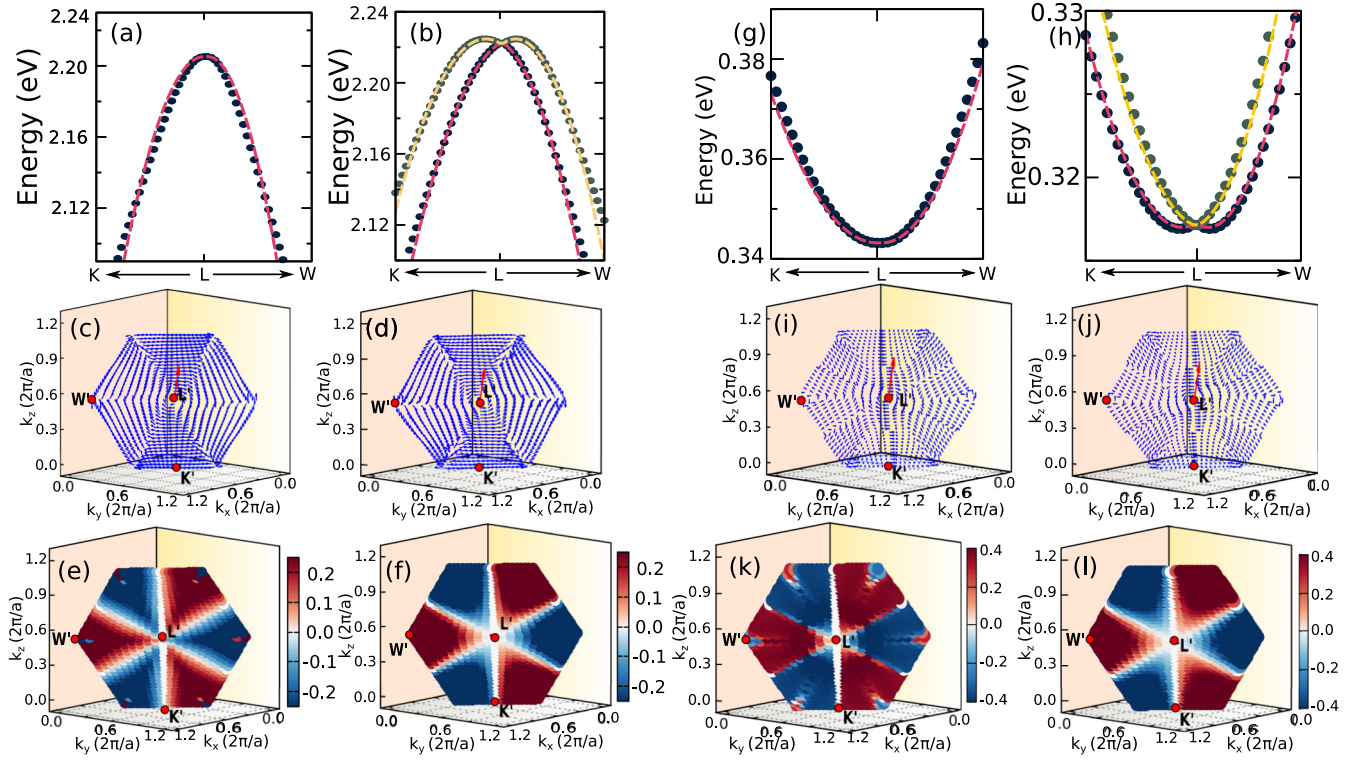


FIG. 5. (a), (b) Band structure without and with SOC for the conduction band for CoZrBi is plotted along  $\frac{2\pi}{a}(0.538, 0.538, 0.425)$ - $\frac{2\pi}{a}(0.5, 0.5, 0.5)$ - $\frac{2\pi}{a}(0.573, 0.427, 0.5)$ , which lies along the path  $K \leftarrow L \rightarrow W$ . The band structure obtained from DFT is plotted with dots, and the band structure obtained from the  $\mathbf{k} \cdot \mathbf{p}$  model Hamiltonian is plotted with dashed lines. (c), (d) ST of inner and outer branches around the  $L'$  point for CoZrBi for the conduction band obtained from DFT calculation. (e), (f) Out-of-plane spin component of CoZrBi in the plane defined by  $k_x + k_y + k_z = \frac{3\pi}{a}$ , obtained from DFT and the model Hamiltonian, respectively. (g), (h) Band structure without and with SOC for the conduction band for SiLiIn is plotted along  $\frac{2\pi}{a}(0.508, 0.508, 0.483)$ - $\frac{2\pi}{a}(0.5, 0.5, 0.5)$ - $\frac{2\pi}{a}(0.516, 0.484, 0.5)$ , which lies along the path  $K \leftarrow L \rightarrow W$ . (i), (j) ST of inner and outer branches around  $L'$  point for SiLiIn in the conduction band. (k), (l) Out-of-plane spin component of SiLiIn in the plane defined by  $k_x + k_y + k_z = \frac{3\pi}{a}$ , obtained from DFT and the model Hamiltonian, respectively.

to the (111) direction in such a way so that  $L$  point is at the origin of this plane given by  $k_x + k_y + k_z = \frac{3\pi}{a}$ . We define a coordinate system such that  $k'_x$  and  $k'_y$  are lying in the plane while  $k'_z$  is along (111) direction. The new coordinate system  $k'_x, k'_y,$  and  $k'_z$  is related to  $k_x, k_y,$  and  $k_z$  by a shift of origin and rotation preserving the local point group symmetry. The resulting unit vectors are  $\hat{k}'_x = \frac{\hat{k}_x}{\sqrt{2}} - \frac{\hat{k}_y}{\sqrt{2}}, \hat{k}'_y = \frac{\hat{k}_x}{\sqrt{6}} + \frac{\hat{k}_y}{\sqrt{6}} - \frac{2\hat{k}_z}{\sqrt{6}}$ , and  $\hat{k}'_z = \frac{1}{\sqrt{3}}\hat{k}_x + \frac{1}{\sqrt{3}}\hat{k}_y + \frac{1}{\sqrt{3}}\hat{k}_z$ . As a consequence, the coordinate of the high-symmetry points in this plane are  $L'(0, 0, 0)$ ,  $W'(\frac{\sqrt{2}\pi}{a}, 0, 0)$ , and  $K'(\frac{\sqrt{6}\pi}{2a}, 0)$ . The corresponding spin textures calculated for the two branches in the above-mentioned plane around the  $L'$  point are shown in Figs. 5(c) and 5(d), respectively. The in-plane spin components exhibit distinct chiral configuration as expected for the Rashba ST, while the presence of the out-of-plane spin components with a distinct pattern [Figs. 5(e) and 5(f)] suggests that higher-order  $k$  terms may be involved. Moving from the inner to the outer branch direction, the chirality changes from clockwise to counterclockwise. In both the inner and outer branches, the spin is orthogonal to the wave vector  $\vec{k}$ , which is typical of Rashba-type SOC. The Rashba parameter estimated from the DFT calculation is found to be  $\alpha_R = 0.37$  eV Å.

The  $\mathbf{k} \cdot \mathbf{p}$  model Hamiltonian is constructed by preserving  $C_{3v}$  symmetry at the  $L$  point. The  $\mathbf{k} \cdot \mathbf{p}$  Hamiltonian is defined in the reciprocal space  $(k'_x, k'_y, k'_z)$  as mentioned above, where the threefold rotation ( $C_3$ ) occurs around the trigonal axis  $k'_z$  (parallel to the [111] direction) in both clockwise ( $C_3^+$ ) and anticlockwise ( $C_3^-$ ) directions. The point group symmetry also includes three mirror planes. One mirror plane lies in the  $k'_y$ - $k'_z$  plane and is defined as  $\sigma''$ , while the other two mirror planes can be obtained by applying  $C_3$  and  $C_3^2$  operations to the initial mirror plane, and they are defined as  $\sigma$  and  $\sigma'$ , respectively. Under these symmetry operations, the momentum and spin operators undergo transformation as listed in Table III. Thus, the symmetry-adapted model Hamiltonian for the conduction band at the  $L$  point is

$$\begin{aligned}
 H_L^C(k) &= H_0(k) + H_{\text{soc}}(k) \\
 &= -\frac{\hbar^2}{2m^*}(k_x^2 + k_y^2) + \alpha_R(\sigma'_y k'_x - \sigma'_x k'_y) \\
 &\quad + \gamma(k_x^3 - 3k_x k_y^2)\sigma'_z.
 \end{aligned} \tag{2}$$

The cubic term in the effective Hamiltonian is included to explain the out-of-plane component  $\sigma'_z$  in the spin texture. The band structure without and with SOC obtained from the model

TABLE III. Symmetry operations of  $C_{3v}$  point group.

Symmetry operation	$\{k'_x, k'_y, k'_z\}$	$\{\sigma'_x, \sigma'_y, \sigma'_z\}$
$C_3^+ ([111]) = e^{-i\frac{2\pi}{3}\sigma'_z}$	$\{(-\frac{1}{2}k'_x + \frac{\sqrt{3}}{2}k'_y), (-\frac{\sqrt{3}}{2}k'_x - \frac{1}{2}k'_y), k'_z\}$	$\{(-\frac{1}{2}\sigma'_x + \frac{\sqrt{3}}{2}\sigma'_y), (-\frac{\sqrt{3}}{2}\sigma'_x - \frac{1}{2}\sigma'_y), \sigma'_z\}$
$C_3^- ([111]) = e^{i\frac{2\pi}{3}\sigma'_z}$	$\{(-\frac{1}{2}k'_x - \frac{\sqrt{3}}{2}k'_y), (\frac{\sqrt{3}}{2}k'_x - \frac{1}{2}k'_y), k'_z\}$	$\{(-\frac{1}{2}\sigma'_x - \frac{\sqrt{3}}{2}\sigma'_y), (\frac{\sqrt{3}}{2}\sigma'_x - \frac{1}{2}\sigma'_y), \sigma'_z\}$
$\sigma = -i(-\frac{1}{2}\sigma'_x + \frac{\sqrt{3}}{2}\sigma'_y)$	$\{(\frac{1}{2}k'_x + \frac{\sqrt{3}}{2}k'_y), (\frac{\sqrt{3}}{2}k'_x - \frac{1}{2}k'_y), k'_z\}$	$\{(-\frac{1}{2}\sigma'_x - \frac{\sqrt{3}}{2}\sigma'_y), (-\frac{\sqrt{3}}{2}\sigma'_x + \frac{1}{2}\sigma'_y), -\sigma'_z\}$
$\sigma' = -i(-\frac{1}{2}\sigma'_x - \frac{\sqrt{3}}{2}\sigma'_y)$	$\{(\frac{1}{2}k'_x - \frac{\sqrt{3}}{2}k'_y), (-\frac{\sqrt{3}}{2}k'_x - \frac{1}{2}k'_y), k'_z\}$	$\{(-\frac{1}{2}\sigma'_x + \frac{\sqrt{3}}{2}\sigma'_y), (\frac{\sqrt{3}}{2}\sigma'_x + \frac{1}{2}\sigma'_y), -\sigma'_z\}$
$\sigma'' = -i\sigma'_x$	$\{-k'_x, k'_y, k'_z\}$	$\{\sigma'_x, -\sigma'_y, -\sigma'_z\}$

Hamiltonian is shown with a dotted line in Figs. 5(a) and 5(b), respectively, and is in good agreement with the DFT band structure. The fitted Rashba parameter  $\alpha_R = 0.38$  eV Å and  $\gamma = -0.32$  eV Å<sup>3</sup> agrees well with the DFT estimate. Further, the out-of-plane component of ST obtained from DFT calculations is in reasonable agreement with that obtained from the model Hamiltonian [see Figs. 4(e) and 4(f)] suggesting the robustness of the low-energy  $\mathbf{k} \cdot \mathbf{p}$  model Hamiltonian [Eq. (2)].

The band structure around the neighborhood of the  $L$  point without and with SOC for the  $s$ - $p$  half-Heusler SiLiIn is presented in Figs. 5(g) and 5(h), respectively. The band structure of the 8-electron compound has a minimum at the  $L$ -point in contrast to a local maximum for the 18-electron compound due to the involvement of  $sp^3$  hybridized state and the calculated Rashba parameter,  $\alpha_R = 0.14$  eV Å, which is much smaller compared to the 18-electron compound. The spin textures of the inner and outer branches around the  $L'$  point of the lowest conduction band are shown in Figs. 5(i) and 5(j). In-plane spin components have a pronounced chiral spin configuration, whereas the presence of the out-of-plane spin component indicates the presence of higher-order  $k$  terms as discussed before for the 18-electron compound [see Figs. 5(k) and 5(l)].

Since the point-group symmetry of SiLiIn is identical to the 18-electron half-Heusler compound CoZrBi, we can easily obtain the model Hamiltonian for the 8-electron system around the  $L'$  point, where  $H_0(k) = \frac{\hbar^2}{2m^*}(k_x^2 + k_y^2)$  and the  $H_{\text{SOC}}$  is identical to Eq. (2). The band structure obtained from the model Hamiltonian agree well with the DFT band dispersion shown with dotted lines in Figs. 5(g) and 5(h). The fitted parameters are  $\alpha_R = 0.15$  eV Å and  $\gamma = -0.51$  eV Å<sup>3</sup>. The obtained Rashba parameter  $\alpha_R$  agrees well with the DFT estimate.

While the model Hamiltonian captures the band dispersion for both compounds accurately, the out-of-plane component of the ST obtained from DFT calculation has additional features that are not reproduced by  $H_L^C$ , suggesting the presence of symmetry-allowed additional terms.

Next we have analyzed the topmost valence bands around the  $L$  point for CoZrBi and SiLiIn that displays a maximum. In the absence of SOC, the threefold-degenerate  $t_2$  bands at the  $\Gamma$  point split into a twofold-degenerate and a singly degenerate band at the  $L$  point, consistent with the  $C_{3v}$  symmetry of the  $L$  point [see Figs. 2(b) and 3(b)]. Inclusion of SOC further splits

the fourfold-degenerate  $J = \frac{3}{2}$  bands at the  $\Gamma$  point into a pair of spin-orbit entangled doubly degenerate  $m_J = \pm\frac{3}{2}$  and  $\pm\frac{1}{2}$  bands at the  $L$ -point with the latter pair of bands lying lower in energy [see Figs. 2(d) and 3(d)]. From Figs. 2(b) and 3(b) we find that the top of the valence band at the  $L$  point for CoZrBi is at the Fermi level, while for SiLiIn it lies about 1.7 eV below the VBM at the  $\Gamma$  point. So in the following we have discussed the SOC-induced band structure and consequent spin texture only for the 18-electron compound CoZrBi.

To obtain further insights, the DFT band dispersion of the topmost valence bands is plotted in a narrow  $k$ -range around the neighborhood of the high-symmetry  $L(\frac{\pi}{a}, \frac{\pi}{a}, \frac{\pi}{a})$  point along the  $W(\frac{2\pi}{a}, 0, \frac{\pi}{a})$  and  $K(\frac{3\pi}{2a}, \frac{3\pi}{2a}, 0)$  directions without and including SOC as shown in Figs. 6(a) and 6(b), respectively. Figure 6(a) reveals a pair of doubly degenerate bands at the  $L$  point and the degeneracy is lifted upon inclusion of SOC [see Fig. 6(b)]. It is interesting to note from Fig. 6(b) that the maxima of the topmost valence bands ( $m_J = \pm\frac{3}{2}$ ) do not bifurcate away from the  $L$  point and remain at the  $L$  point, while for the lower two bands ( $m_J = \pm\frac{1}{2}$ ) the maxima are bifurcated away from the  $L$  point displaying band crossing as expected for the linear Rashba effect. This clearly establishes the absence of the linear Rashba effect for the topmost valence bands, and therefore the leading term of the SOC Hamiltonian for the topmost bands is expected to be cubic [25,42]. Such pure cubic Rashba splitting for  $m_J = \pm\frac{3}{2}$  bands has also been observed experimentally in strained Ge [43].

The plot of the DFT spin textures for the two bands around the  $L'$  point is illustrated in Figs. 6(c) and 6(d). Our calculations reveal that the in-plane spin-component exhibits a characteristic chiral configuration with the presence of a substantial out-of-plane spin component as illustrated in Fig. 6(e). In fact, the out-of-plane component dominates over the in-plane component of  $\langle \vec{S} \rangle$ .

To corroborate our DFT results, a  $\mathbf{k} \cdot \mathbf{p}$  model Hamiltonian is constructed with cubic Rashba as the leading term respecting the  $C_{3v}$  symmetry at the  $L$  point [25]. The symmetry-adapted low-energy  $\mathbf{k} \cdot \mathbf{p}$  model Hamiltonian is

$$H_L^v(k) = H_0(k) + \gamma(k_x^3 - 3k'_x k_y^2)\sigma'_z + \delta((k_x^3 + k'_x k_y^2)\sigma'_y - (k_y^3 + k'_y k_x^2)\sigma'_x). \quad (3)$$

The band structure without and with SOC obtained from the model Hamiltonian for the topmost two bands is shown with a dotted line in Figs. 6(a) and 6(b), respectively, and is in good agreement with DFT results. The calculated parame-

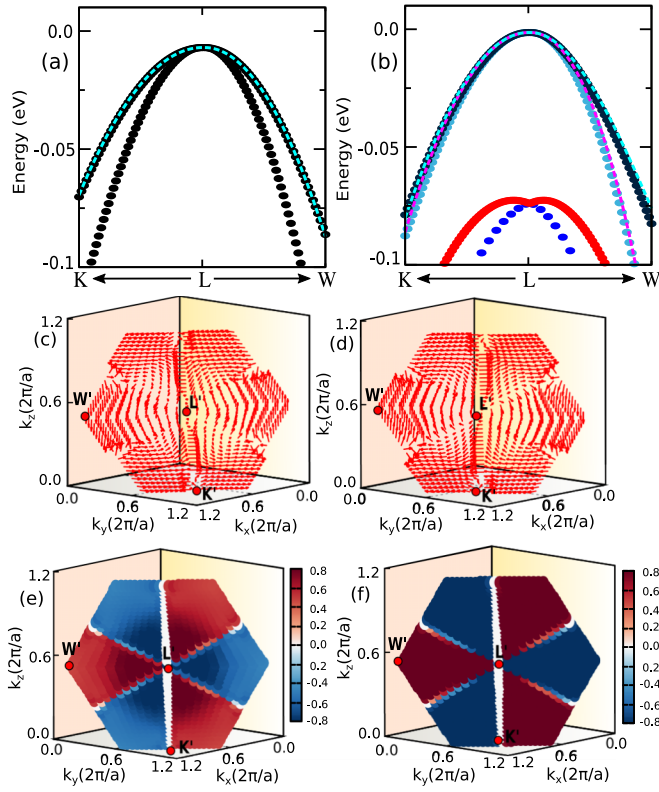


FIG. 6. (a), (b) Band structure without and with SOC for the valence-band maxima for CoZrBi is plotted along  $\frac{2\pi}{a}(0.563, 0.563, 0.374)$ - $\frac{2\pi}{a}(0.5, 0.5, 0.5)$ - $\frac{2\pi}{a}(0.623, 0.377, 0.5)$  which lies along the path  $K \leftarrow L \rightarrow W$ . The band structure obtained from DFT is plotted with dots, and the band structure obtained from the  $\mathbf{k} \cdot \mathbf{p}$  model Hamiltonian is plotted with dashed lines. (c), (d) ST of inner and outer branches around the  $L'$  point for CoZrBi for the conduction band obtain from DFT calculation. (e), (f) Out-of-plane spin component of CoZrBi in the plane defined by  $k_x + k_y + k_z = \frac{3\pi}{a}$ , obtained from DFT and the model Hamiltonian, respectively.

ters of the model Hamiltonian are  $\gamma = 5.5 \text{ eV}\text{\AA}^3$  and  $\delta = 0.9 \text{ eV}\text{\AA}^3$  emphasizing the importance of the out-of-plane spin component. The out-of-plane component of the spin texture obtained from the model Hamiltonian shown in Fig. 6(f) is in reasonable agreement with the DFT spin texture shown in Fig. 6(e). The discovery of pure cubic Rashba splitting in nonpolar half-Heusler alloys is rather unique and expected to find application in spintronics.

Similar results are obtained for the 8-electron compound SiLiIn where the splitting of the bands as expected is small.

## B. Zeeman spin splitting

Up to now we have discussed spin splitting and consequent spin textures around the time reversal invariant  $k$ -points. Here we shall consider spin textures around the non-time-reversal invariant  $W$  point. The band structure of the top of the valence band of CoZrBi around the  $W(\frac{\pi}{a}, \frac{2\pi}{a}, 0)$  point along the path  $X(0, \frac{2\pi}{a}, 0)$  and  $K(\frac{3\pi}{2a}, \frac{3\pi}{2a}, 0)$  all lying in the  $k_x$ - $k_y$  plane without and including spin orbit coupling is displayed

in Figs. 7(a) and 7(b), respectively. We find that the spin degeneracy of the bands is lifted upon inclusion of SOC. In contrast to the Rashba and Dresselhaus effect, the spin splitting around the non-time-reversal invariant  $W$  point does not have band crossing, rather the splitting is identical to that realized in magnetic systems (i.e., in the absence of time-reversal symmetry). Interestingly, such a splitting is now realized in a nonmagnetic system in the absence of inversion symmetry around a non-time-reversal invariant high-symmetry  $W$  point and will be designated as Zeeman splitting. It may be noted that while the band structure around the  $W$  point in the  $k_x$ - $k_y$  plane along the path  $X$ - $W$ - $K$  is identical to that plotted along  $X(0, \frac{2\pi}{a}, 0)$ - $W(0, \frac{2\pi}{a}, \frac{\pi}{a})$ - $K(0, \frac{3\pi}{2a}, \frac{3\pi}{2a})$  lying in the  $k_y$ - $k_z$  plane, the ST of the bands, however, are dominated by different spin components depending on the chosen plane. This is illustrated in Figs. 7(c)–7(e) for the  $k_x$ - $k_y$  plane and Figs. 7(f)–7(h) for the  $k_y$ - $k_z$  plane where the primary contribution to the ST is from  $S_x$  and  $S_z$  components, respectively.

To explain the above observation, we have calculated the effective SOC term allowed by symmetry around the  $W$  point. The point group symmetry around the  $W$  point is  $S_4$ , which contains a twofold rotation ( $C_2$ ) around the principal axis. Additionally, there are two fourfold rotations ( $C_4$ ) around the principal axis, one in the clockwise direction ( $C_4^+$ ) and the other in the anticlockwise direction ( $C_4^-$ ), followed by a reflection. The SOC term and the resulting SOC Hamiltonian [29] under the symmetry is

$$\Omega_Z(k) = \lambda_Z [k_x(k_y^2 - k_z^2), k_y(k_z^2 - k_x^2), k_z(k_x^2 - k_y^2)]$$

$$H_W = \Omega_Z(\mathbf{k}) \cdot \boldsymbol{\sigma}, \quad (4)$$

where  $\lambda_Z$  is the Zeeman parameter. At the  $W$  point the splitting of the top two bands of CoZrBi is 186 meV as revealed from our DFT calculations. As the  $W$  point lies at the boundary of the BZ, from the above Hamiltonian we can easily understand that the effective magnetic field is more at the boundary, causing a large splitting. To understand the origin of SOC-induced different spin textures in different planes, we need to understand the symmetry associated with the chosen paths in the reciprocal space. The symmetry operations around the  $W$  point in the  $k_x$ - $k_y$  plane along  $X(0, \frac{2\pi}{a}, 0)$ - $W(\frac{\pi}{a}, \frac{2\pi}{a}, 0)$  are  $C_{2x}$ . The spin components under the symmetry operation  $C_{2x}$  transform like,  $C_{2x} : (\sigma_x, \sigma_y, \sigma_z) \rightarrow (\sigma_x, -\sigma_y, -\sigma_z)$ , ensuring primarily the  $\sigma_x$  component survives in the Hamiltonian. Using the model Hamiltonian in the  $k_x$ - $k_y$  plane with  $k_z = 0$ , we focus on the  $X(0, \frac{2\pi}{a}, 0) \rightarrow W(\frac{\pi}{a}, \frac{2\pi}{a}, 0)$  direction, where  $k_y$  is fixed and only  $k_x$  changes. This leads to an effective Hamiltonian around the  $W$  point and along the path  $XW$ , given by  $H_W = \lambda_Z k_x k_y^2 \sigma_x$ , assuming ( $k_x \ll k_y = \frac{2\pi}{a}$ ). This suggests that the spin expectation value will be mostly contributed by the  $S_x$  component having a positive value for the upper valence band around the  $W$  point, and negative for the lower valence band in agreement with DFT calculations shown in Figs. 7(c)–7(e). Similarly for the  $k_y$ - $k_z$  plane, the Hamiltonian with ( $k_z \ll k_y = \frac{2\pi}{a}$ ) will be given by  $H_W = -\lambda_Z k_z k_y^2 \sigma_z$ , as we move along the  $X(0, \frac{2\pi}{a}, 0) \rightarrow W(0, \frac{2\pi}{a}, \frac{\pi}{a})$  direction where the valence band primarily has  $\sigma_z$  character. Here the expectation value of  $\langle S_z \rangle$  is negative for the top of the valence band, while it is positive for the lower valence band, in agreement with our DFT results.



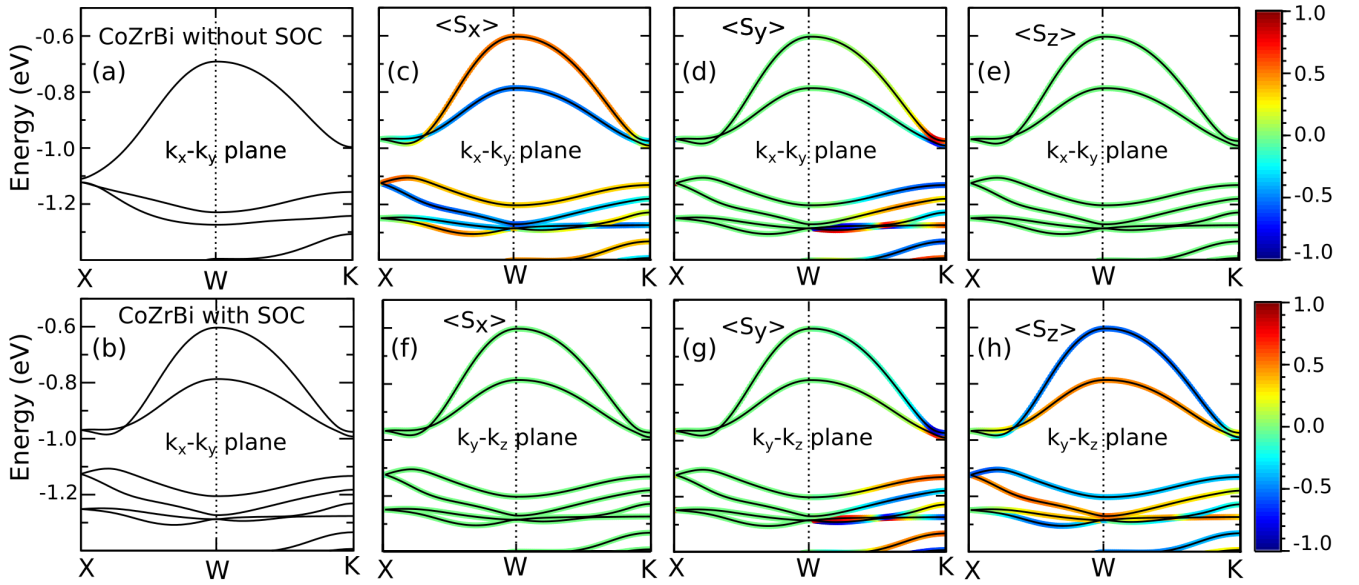


FIG. 7. Figure shows the band structure along with projected spin textures at non-time-reversal invariant  $k$ -point  $W$  of CoZrBi. Panels (a) and (b) show the band structure of CoZrBi without and with SOC along the path  $X(0, \frac{2\pi}{a}, 0)$ -  $W(\frac{\pi}{a}, \frac{2\pi}{a}, 0)$ -  $K(\frac{3\pi}{2a}, \frac{3\pi}{2a}, 0)$ . Panels [(c)-(e)] show the band structure with projected spin textures in the presence of SOC for CoZrBi along the path  $X(0, \frac{2\pi}{a}, 0)$ -  $W(\frac{\pi}{a}, \frac{2\pi}{a}, 0)$ -  $K(\frac{3\pi}{2a}, \frac{3\pi}{2a}, 0)$  in the  $k_x - k_y$  plane. Panels [(f)-(h)] show the band structure and spin textures in presence of SOC for CoZrBi along the path  $X(0, \frac{2\pi}{a}, 0)$ -  $W(0, \frac{2\pi}{a}, \frac{\pi}{a})$ -  $K(0, \frac{3\pi}{2a}, \frac{3\pi}{2a})$  in the  $k_y - k_z$  plane. The color code represents the orientation of the spin component.

The results of our calculation for the 8-electron half-Heusler compound are shown in Fig. 8. A pair of valence bands around the  $W$  point exhibit Zeeman splitting upon application of SOC, where the splitting is more for the lower pair of bands. It should be noted that splitting is weak in comparison to the 18-electron compound. Further, the nature of the spin textures is quite different from the 18-electron compound. In contrast to the 18-electron compound in the  $k_x$ - $k_y$  plane, in addition to the  $\langle S_x \rangle$  component there is appreciable  $\langle S_y \rangle$  character [see Figs. 8(c)–8(e)]. Similarly in the  $k_y$ - $k_z$  plane in addition to the  $\langle S_z \rangle$  character, the  $\langle S_y \rangle$  character is also present [see Figs. 8(f)–8(h)].

### C. Band splitting with vanishing spin polarization (BSVSP)

The two half-Heusler systems considered here also exhibit another intriguing phenomenon, namely band splitting with vanishing spin polarization, where SOC splits the energy bands, however neither of the split bands exhibits net spin polarization along certain high-symmetry directions of the BZ due to the presence of additional symmetries. In Fig. 9(a) the top of the valence band without SOC for CoZrBi along the path  $A(\frac{\pi}{a}, \frac{\pi}{2a}, 0)$ - $\Gamma(0, 0, 0)$ - $L(\frac{\pi}{a}, \frac{\pi}{a}, \frac{\pi}{a})$  is displayed. In the absence of SOC, the  $T_d$  symmetry at the  $\Gamma$  point splits the  $d$  bands into twofold-degenerate  $e$  and threefold-degenerate  $t_2$  states. In Fig. 9(b) the same band structure including SOC is displayed. Inclusion of SOC further splits the  $t_2$  states into twofold-degenerate  $J = \frac{1}{2}$  and fourfold-degenerate  $J = \frac{3}{2}$  states, with the  $J = \frac{1}{2}$  states lying lower in energy. Along the symmetry line  $\Gamma$ - $L$  the  $J = \frac{3}{2}$  states further split into three bands, where the lowest of the three is doubly degenerate. In Fig. 9(c) we have shown the band structure projecting the  $\langle S_x \rangle$  component of the spin. The expectation value of  $\langle S_x \rangle$  vanishes

for the top two spin split bands along  $\Gamma$ - $L$  and the same is true for the other spin components. The vanishing expectation value of the spin  $\langle \vec{S} \rangle$  for the two nondegenerate bands along  $\Gamma$ - $L$  over each Bloch wave function leads to BSVSP.

To understand the origin of the vanishing spin polarization, we have constructed a  $\mathbf{k} \cdot \mathbf{p}$  model Hamiltonian following Refs. [7,44]. The  $\mathbf{k} \cdot \mathbf{p}$  Hamiltonian for the  $J = \frac{3}{2}$  manifold of the top of the valence band for the 18-electron compound CoZrBi in the vicinity of the  $\Gamma$  point may be written as  $H = H^+ + H^-$ , where  $H^+$  is invariant with respect to the spatial inversion,

$$H^+ = \frac{\hbar^2}{m} \left[ \left( \gamma_1 + \frac{5}{2} \gamma_2 \right) \frac{1}{2} k^2 - \gamma_2 (k_x^2 J_x^2 + k_y^2 J_y^2 + k_z^2 J_z^2) \right] - 2\gamma_3 (\{k_x, k_y\} \{J_x, J_y\} + \{k_y, k_z\} \{J_y, J_z\} + \{k_z, k_x\} \{J_z, J_x\}) \quad (5)$$

and  $H^-$  breaks the spatial inversion symmetry,

$$H^- = -\frac{2C}{\sqrt{3}} [k_x \{J_x, V_x\} + k_y \{J_y, V_y\} + k_z \{J_z, V_z\}]. \quad (6)$$

Here,  $\gamma_1$ ,  $\gamma_2$ ,  $\gamma_3$ , and  $c$  are constants.  $J_x$ ,  $J_y$ , and  $J_z$  are  $4 \times 4$  angular momentum matrices for a state of spin  $\frac{3}{2}$ , and  $k_x$ ,  $k_y$ , and  $k_z$  are the kinetic momentum terms. The symbol  $\{a, b\}$  means the symmetrized product  $\frac{1}{2}(ab + ba)$ . The quantities  $V_x$ ,  $V_y$ , and  $V_z$  are given by  $V_x = J_y^2 - J_z^2$ ,  $V_y = J_z^2 - J_x^2$ ,  $V_z = J_x^2 - J_y^2$ . Here, we focus on the band degeneracy and spin polarization instead of the exact band dispersion. The DFT band structure in a narrow range around the  $\Gamma$  point along the path  $A$ - $\Gamma$ - $L$  can be reasonably reproduced, with the fitted parameter values  $\gamma_1 = -9.0$ ,  $\gamma_2 = 2.0$ ,  $\gamma_3 = -1.9$ ,  $\frac{\hbar^2}{m} = 1$ , and  $C = -0.05$  [see Fig. 9(c) inset]. The qualitative results do not depend on the exact parameters. To investigate the

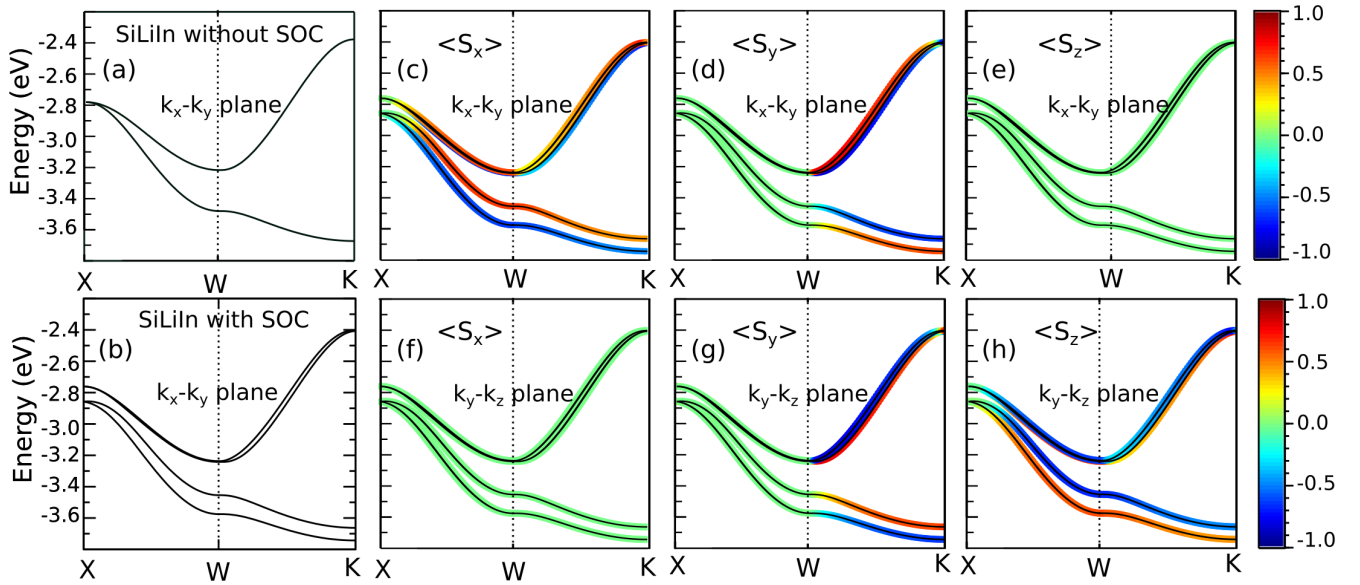


FIG. 8. Band structure along with projected spin texture at non-time-reversal invariant  $k$ -point  $W$  of SiLiIn. Panels (a) and (b) show the band structure of SiLiIn without and with SOC along the path  $X(0, \frac{2\pi}{a}, 0)-W(\frac{2\pi}{a}, \frac{\pi}{a}, 0)-K(\frac{3\pi}{2a}, \frac{3\pi}{2a}, 0)$ . Panels [(c)–(e)] show the band structure with projected spin textures in the presence of SOC for SiLiIn along the path  $X(0, \frac{2\pi}{a}, 0)-W(\frac{\pi}{a}, \frac{2\pi}{a}, 0)-K(\frac{3\pi}{2a}, \frac{3\pi}{2a}, 0)$  in the  $k_x$ - $k_y$  plane. Panels [(f)–(h)] show the band structure and spin textures in presence of SOC for SiLiIn along the path  $X(0, \frac{2\pi}{a}, 0)-W(0, \frac{2\pi}{a}, \frac{\pi}{a})-K(0, \frac{3\pi}{2a}, \frac{3\pi}{2a})$  in the  $k_y$ - $k_z$  plane. The color code represents the orientation of the spin component.

microscopic origin of the vanishing spin polarization along the symmetry line  $\Gamma$ - $L$ , we have calculated the on-site energy differences between the orbitals of two nondegenerate  $t_2$  states with opposite spin orientations, which can be regarded as the magnetic field acting locally on the chosen orbitals. From the calculations we find that the magnetic field on a given orbital vanishes. The local magnetic moments associated with these orbitals cancel with each other, resulting in a vanishing net spin polarization for the eigenstate and vanishing local spin polarization for the magnetic Co atom. In agreement with the DFT results, the projection of the  $\langle S_x \rangle$  component on the band structure obtained from the model Hamiltonian also vanishes supporting the validity of the low-energy model Hamiltonian.

Similar results around the  $\Gamma$  point and along the path  $\Gamma$ - $L$  are displayed by the 8-electron compound SiLiIn. In Fig. 9(d) the band structure without SOC is threefold-degenerate around the  $\Gamma$  point. Inclusion of SOC splits the threefold-degenerate  $t_2$  bands into a  $J = \frac{3}{2}$  quartet and a  $J = \frac{1}{2}$  doublet as shown in Fig. 9(e). The splitting induced by SOC is 0.10 eV. Along the path  $\Gamma$ - $L$ , the top  $J = \frac{3}{2}$  bands further split into a pair of nondegenerate bands and a doubly degenerate band, and the former exhibit the BSVSP effect along  $\Gamma$ - $L$ . The splitting is, however, much smaller in comparison to the 18-electron compound [see the inset of Fig. 9(f)].

Using the same model Hamiltonian as described for the 18-electron half-Heusler, we can understand the origin of the BSVSP for SiLiIn. We find the SOC-induced effective magnetic field acting on two different  $p$  orbitals of the same atom is equal and opposite in strength along the  $\Gamma L$  path, resulting in a BSVSP [7]. The splitting of the bands depends on the strength of SOC. As a consequence, the BSVSP effect is much stronger (30 meV) for the 18-electron compound while it is 3 meV for the 8-electron compound SiLiIn and only 0.05 meV for GaAs, suggesting 18-electron com-

pounds will be ideal candidates for experimental detection of BSVSP.

## V. CONCLUSION

In the present paper, we have analyzed the electronic structure of two representative half-Heusler systems with 18 electrons and 8 electrons, respectively, in the presence of spin-orbit interaction. Our calculations reveal rich features in the electronic structure due to spin-momentum locking induced by SOC. Although both compounds have identical crystal structure, the orbital composition of the valence and conduction bands is different for the 18-electron and the 8-electron system. This brings in subtle changes in the SOC-induced band structures, emphasizing the important role of orbitals. In addition, the BZ of the half-Heusler system admits diverse local symmetries (little group) leading to nontrivial splitting of the band structure due to SOC, resulting in novel spin textures around the valleys of the high-symmetry  $k$ -points.

Around the  $X$  point we have observed the Dresselhaus effect as expected for a noncentrosymmetric and nonpolar material [45] (see Table IV). Using a symmetry-adapted  $\mathbf{k} \cdot \mathbf{p}$  model Hamiltonian around the high-symmetry  $X$  point, we have calculated the band dispersion and the consequent ST. The model Hamiltonian only required linear terms to reproduce the DFT results, and the Dresselhaus parameter  $\alpha_D$  for the 18-electron and the 8-electron system is calculated to be 0.26 and 0.08 eVÅ respectively, in good agreement with DFT results.

Similar to the Dresselhaus effect, we have observed the Rashba effect in both half-Heusler systems around the polar  $L(\frac{\pi}{a}, \frac{\pi}{a}, \frac{\pi}{a})$  point in the [111] plane. The Rashba effect features both linear and higher-order terms for the conduction

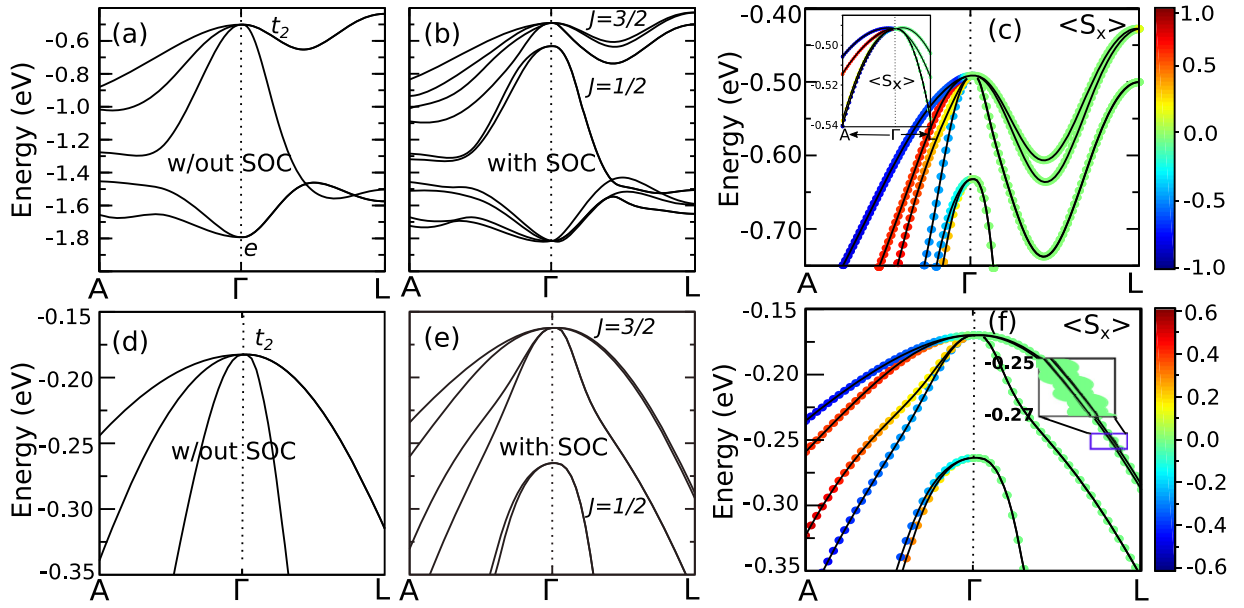


FIG. 9. Band splitting with vanishing spin polarization for 18- and 8-electron half-Heusler compounds. Panels (a) and (b) show the band structure of CoZrBi without and with SOC along the path  $A(\frac{2\pi}{a}0.5, \frac{2\pi}{a}0.25, 0.0)-\Gamma(0, 0, 0)-L(\frac{2\pi}{a}0.5, \frac{2\pi}{a}0.5, \frac{2\pi}{a}0.5)$ . Panels (d) and (e) show the band structure of SiLiIn without and with SOC along the path  $A(\frac{2\pi}{a}0.5, \frac{2\pi}{a}0.25, 0.0)-\Gamma(0, 0, 0)-L(\frac{2\pi}{a}0.5, \frac{2\pi}{a}0.5, \frac{2\pi}{a}0.5)$ . Panels (c) and (f) show the band structure and the  $x$  component of spin polarization for 18-electron and 8-electron compounds obtained from DFT. The inset of (c) represents the band structure and the  $x$  component of spin polarization obtained from  $\mathbf{k} \cdot \mathbf{p}$  model Hamiltonian.

band, but the strength of the higher-order term is found to be much weaker compared to the linear term. However, for the topmost valence band at the  $L$  point we have identified cubic Rashba to be the leading term of the SOC Hamiltonian with novel spin texture. The identification of pure cubic Rashba splitting in half-Heusler alloys is rather unique and is expected

TABLE IV. Our result and available Rashba and Dresselhaus parameters in the literature.

System	$\alpha_R(\text{eV}\text{\AA})$ $k$ -point	$\alpha_D(\text{eV}\text{\AA})$ $k$ -point	Nonpolar or polar	Reference
CoZrBi	0.38 $L(\frac{\pi}{a}, \frac{\pi}{a}, \frac{\pi}{a})$	0.26 $X(0, 0, \frac{2\pi}{a})$	Nonpolar	This work
SiLiIn	0.15 $L(\frac{\pi}{a}, \frac{\pi}{a}, \frac{\pi}{a})$	0.08 $X(0, 0, \frac{2\pi}{a})$	Nonpolar	This work
BiTeI	3.8 $\Gamma(0, 0, 0)$	0.00 $\Gamma(0, 0, 0)$	Polar	[18]
GeTe	4.8 $Z(\frac{\pi}{a}, \frac{\pi}{a}, \frac{\pi}{a})$	0.00 $Z(\frac{\pi}{a}, \frac{\pi}{a}, \frac{\pi}{a})$	Polar	[21]
HfO <sub>2</sub>	0.028 $T(0, \frac{\pi}{b}, \frac{\pi}{c})$	0.578 $T(0, \frac{\pi}{b}, \frac{\pi}{c})$	Polar	[24]
LaWN <sub>3</sub>	0.31 $\Gamma(0, 0, 0)$	0.01 $\Gamma(0, 0, 0)$	Polar	[25]
AlAs	0.00 $X(0, 0, \frac{2\pi}{a})$	0.01 $X(0, 0, \frac{2\pi}{a})$	Nonpolar	[45]
GaP	0.00 $X(0, 0, \frac{2\pi}{a})$	0.07 $X(0, 0, \frac{2\pi}{a})$	Nonpolar	[45]

to play an important role in spin transport. Further, both Dresselhaus and Rashba splitting are found to be much weaker for the 8-electron  $sp$ -based compound in comparison to the 18-electron system.

At the non-TR invariant high-symmetry point  $W$ , we observe Zeeman spin splitting. From the  $\mathbf{k} \cdot \mathbf{p}$  model Hamiltonian, we have established that only the cubic terms are invariant under symmetry operations, and the component of spin orientation depends on the chosen plane.

Finally, we have observed the BSVSP along the high-symmetry path  $\Gamma$ - $L$  in both 18-electron and 8-electron half-Heusler systems. Around the  $\Gamma$  point, the tetrahedral environment causes the  $d$  orbitals of the 18 electron half-Heusler to split into  $t_2$  and  $e$  states while leaving the  $p$  states degenerate for the 8-electron half-Heusler compound. The SOC further splits the  $t_2$  and  $p$  states into fourfold-degenerate  $J = \frac{3}{2}$  and twofold-degenerate  $J = \frac{1}{2}$  states. Along the path  $\Gamma$ - $L$  the fourfold-degenerate  $J = \frac{3}{2}$  states further split into two nondegenerate bands and a twofold-degenerate band. The presence of a pair of nondegenerate bands in the presence of SOC with the little group of the relevant  $k$ -point belonging to the non-pseudo-polar point group leads to BSVSP [7].

Our calculations reveal that the valence band and the conduction band of half-Heusler alloys at the various high-symmetry points feature extrema (valleys) characterized by spin texture, which are dependent on the location of the valleys in the  $k$ -space designated by a valley index. In the presence of SOC, the spin splitting is tied to the valley index, requiring the scattering of charge carriers between valleys to have simultaneous spin flip and momentum transfer. This

favors the long valley lifetime required for valleytronics application. These valleys can be accessible by doping.

Our detailed first-principles calculations complemented with the  $k \cdot p$  model Hamiltonian method for the two representative half-Heusler systems identify in a family of ternary half-Heusler system with heavy elements another novel functionality for potential application in spin-valleytronics [46].

## ACKNOWLEDGMENTS

K.D. thanks the Council of Scientific and Industrial Research (CSIR) for support through a fellowship [File No. 09/080(1178)/2020-EMR-I]. I.D. thanks Science and Engineering Research Board (SERB) India (Project No. CRG/2021/003024) and Technical Research Center, Department of Science and Technology (TRC-DST) for support.

- 
- [1] E. I. Rashba, *Sov. Phys. Solid State* **2**, 1109 (1960).
- [2] G. Dresselhaus, *Phys. Rev.* **100**, 580 (1955).
- [3] B. A. Bernevig, J. Orenstein, and S.-C. Zhang, *Phys. Rev. Lett.* **97**, 236601 (2006).
- [4] M. Hirayama, R. Okugawa, S. Ishibashi, S. Murakami, and T. Miyake, *Phys. Rev. Lett.* **114**, 206401 (2015).
- [5] P. Zeeman, *Nature (London)* **55**, 347 (1897).
- [6] Y. Li, J. Ludwig, T. Low, A. Chernikov, X. Cui, G. Arefe, Y. D. Kim, A. M. van der Zande, A. Rigosi, H. M. Hill, S. H. Kim, J. Hone, Z. Li, D. Smirnov, and T. F. Heinz, *Phys. Rev. Lett.* **113**, 266804 (2014).
- [7] K. Liu, W. Luo, J. Ji, P. Barone, S. Picozzi, and H. Xiang, *Nat. Commun.* **10**, 5144 (2019).
- [8] G. Bihlmayer, O. Rader, and R. Winkler, *New J. Phys.* **17**, 050202 (2015).
- [9] S. LaShell, B. A. McDougall, and E. Jensen, *Phys. Rev. Lett.* **77**, 3419 (1996).
- [10] Y. M. Koroteev, G. Bihlmayer, J. E. Gayone, E. V. Chulkov, S. Blügel, P. M. Echenique, and P. Hofmann, *Phys. Rev. Lett.* **93**, 046403 (2004).
- [11] H. Nakamura, T. Koga, and T. Kimura, *Phys. Rev. Lett.* **108**, 206601 (2012).
- [12] P. D. C. King, R. H. He, T. Eknapakul, P. Buaphet, S.-K. Mo, Y. Kaneko, S. Harashima, Y. Hikita, M. S. Bahramy, C. Bell, Z. Hussain, Y. Tokura, Z.-X. Shen, H. Y. Hwang, F. Baumberger, and W. Meevasana, *Phys. Rev. Lett.* **108**, 117602 (2012).
- [13] Y. C. Cheng, Z. Y. Zhu, M. Tahir, and U. Schwingenschlogl, *Europhys. Lett.* **102**, 57001 (2013).
- [14] H. L. Zhuang, V. R. Cooper, H. Xu, P. Ganesh, R. G. Hennig, and P. R. C. Kent, *Phys. Rev. B* **92**, 115302 (2015).
- [15] Z. S. Popović, J. M. Kurdestany, and S. Satpathy, *Phys. Rev. B* **92**, 035135 (2015).
- [16] J. Nitta, T. Akazaki, H. Takayanagi, and T. Enoki, *Phys. Rev. Lett.* **78**, 1335 (1997).
- [17] A. D. Caviglia, M. Gabay, S. Gariglio, N. Reyren, C. Cancellieri, and J.-M. Triscone, *Phys. Rev. Lett.* **104**, 126803 (2010).
- [18] K. Ishizaka, M. S. Bahramy, H. Murakawa, M. Sakano, T. Shimojima, T. Sonobe, K. Koizumi, S. Shin, H. Miyahara, A. Kimura, K. Miyamoto, T. Okuda, H. Namatame, M. Taniguchi, R. Arita, N. Nagaosa, K. Kobayashi, Y. Murakami, R. Kumai, Y. Kaneko *et al.*, *Nat. Mater.* **10**, 521 (2011).
- [19] M. Sakano, M. S. Bahramy, A. Katayama, T. Shimojima, H. Murakawa, Y. Kaneko, W. Malaeb, S. Shin, K. Ono, H. Kumigashira, R. Arita, N. Nagaosa, H. Y. Hwang, Y. Tokura, and K. Ishizaka, *Phys. Rev. Lett.* **110**, 107204 (2013).
- [20] F.-X. Xiang, X.-L. Wang, M. Veldhorst, S.-X. Dou, and M. S. Fuhrer, *Phys. Rev. B* **92**, 035123 (2015).
- [21] D. Di Sante, P. Barone, R. Bertacco, and S. Picozzi, *Adv. Mater.* **25**, 509 (2013).
- [22] M. Liebmann, C. Rinaldi, D. Di Sante, J. Kellner, C. Pauly, R. N. Wang, J. E. Boschker, A. Giussani, S. Bertoli, M. Cantoni, L. Baldrati, M. Asa, I. Vobornik, G. Panaccione, D. Marchenko, J. Sánchez-Barriga, O. Rader, R. Calarco, S. Picozzi, R. Bertacco *et al.*, *Adv. Mater.* **28**, 560 (2016).
- [23] L. G. D. da Silveira, P. Barone, and S. Picozzi, *Phys. Rev. B* **93**, 245159 (2016).
- [24] L. L. Tao, T. R. Paudel, A. A. Kovalev, and E. Y. Tsymbal, *Phys. Rev. B* **95**, 245141 (2017).
- [25] S. Bandyopadhyay, A. Paul, and I. Dasgupta, *Phys. Rev. B* **101**, 014109 (2020).
- [26] C. Mera Acosta, L. Yuan, G. M. Dalpian, and A. Zunger, *Phys. Rev. B* **104**, 104408 (2021).
- [27] H. Yuan, M. S. Bahramy, K. Morimoto, S. Wu, K. Nomura, B.-J. Yang, H. Shimotani, R. Suzuki, M. Toh, C. Kloc, X. Xu, R. Arita, N. Nagaosa, and Y. Iwasa, *Nat. Phys.* **9**, 563 (2013).
- [28] D. Xiao, G.-B. Liu, W. Feng, X. Xu, and W. Yao, *Phys. Rev. Lett.* **108**, 196802 (2012).
- [29] C. Mera Acosta, A. Fazzio, and G. M. Dalpian, *npj Quantum Mater.* **4**, 41 (2019).
- [30] J.-W. Luo, G. Bester, and A. Zunger, *Phys. Rev. Lett.* **102**, 056405 (2009).
- [31] S. Bandyopadhyay and I. Dasgupta, *Phys. Rev. B* **103**, 014105 (2021).
- [32] M. Yazdani-Kachoei and S. Jalali-Asadabadi, *J. Alloys Compd.* **828**, 154287 (2020).
- [33] Vikram, B. Sahni, C. K. Barman, and A. Alam, *J. Phys. Chem. C* **123**, 7074 (2019).
- [34] G. Kresse and J. Hafner, *Phys. Rev. B* **47**, 558 (1993).
- [35] G. Kresse and J. Furthmüller, *Phys. Rev. B* **54**, 11169 (1996).
- [36] P. E. Blöchl, *Phys. Rev. B* **50**, 17953 (1994).
- [37] G. Kresse and D. Joubert, *Phys. Rev. B* **59**, 1758 (1999).
- [38] J. P. Perdew, K. Burke, and M. Ernzerhof, *Phys. Rev. Lett.* **77**, 3865 (1996).
- [39] S. Vajna, E. Simon, A. Szilva, K. Palotas, B. Ujjfalussy, and L. Szunyogh, *Phys. Rev. B* **85**, 075404 (2012).
- [40] B. R. K. Nanda and I. Dasgupta, *J. Phys.: Condens. Matter* **15**, 7307 (2003).
- [41] H. Zhu, R. He, J. Mao, Q. Zhu, C. Li, J. Sun, W. Ren, Y. Wang, Z. Liu, Z. Tang, A. Sotnikov, Z. Wang, D. Broido, D. J. Singh, G. Chen, K. Nielsch, and Z. Ren, *Nat. Commun.* **9**, 2497 (2018).

- [42] H. J. Zhao, H. Nakamura, R. Arras, C. Paillard, P. Chen, J. Gosteau, X. Li, Y. Yang, and L. Bellaiche, *Phys. Rev. Lett.* **125**, 216405 (2020).
- [43] R. Moriya, K. Sawano, Y. Hoshi, S. Masubuchi, Y. Shiraki, A. Wild, C. Neumann, G. Abstreiter, D. Bougeard, T. Koga, and T. Machida, *Phys. Rev. Lett.* **113**, 086601 (2014).
- [44] C. R. Pidgeon and S. H. Groves, *Phys. Rev.* **186**, 824 (1969).
- [45] S. Mishra, S. Thulasi, and S. Satpathy, *Phys. Rev. B* **72**, 195347 (2005).
- [46] F. Casper, T. Graf, S. Chadov, B. Balke, and C. Felser, *Semicond. Sci. Technol.* **27**, 063001 (2012).